Corrosion Science 195 (2022) 109962

Contents lists available at ScienceDirect

Corrosion Science

journal homepage: www.elsevier.com/locate/corsci

Visualizing time-dependent microstructural and chemical evolution during molten salt corrosion of Ni-20Cr model alloy using correlative *quasi in situ* TEM and *in situ* synchrotron X-ray nano-tomography

Kaustubh Bawane [a,*], Xiaoyang Liu [b], Ruchi Gakhar [c], Michael Woods [c], Mingyuan Ge [d], Xianghui Xiao [d], Wah-Keat Lee [d], Philip Halstenberg [e,f], Sheng Dai [e,f], Shannon Mahurin [e], Simon M. Pimblott [g], James F. Wishart [h], Yu-chen Karen Chen-Wiegart [b,d,**], Lingfeng He [a,*]

[a] *Advanced Characterization Department, Idaho National Laboratory, Idaho Falls, ID 83415, USA*
[b] *Department of Materials Science and Chemical Engineering, Stony Brook University, Stony Brook, NY 11794, USA*
[c] *Pyrochemistry and Molten Salt Systems Department, Idaho National Laboratory, Idaho Falls, ID, 83415, USA*
[d] *National Synchrotron Light Source II (NSLS-II), Brookhaven National Laboratory, Upton, NY, 11973, USA*
[e] *Chemical Sciences Division, Oak Ridge National Laboratory, Oak Ridge, TN, 37830, USA*
[f] *Department of Chemistry, University of Tennessee, Knoxville, TN, 37996, USA*
[g] *Nuclear Science User Facilities, Idaho National Laboratory, Idaho Falls, ID, 83415, USA*
[h] *Chemistry Division, Brookhaven National Laboratory, Upton, NY, 11973, USA*

ARTICLE INFO

Keywords:
Molten salt corrosion
quasi in situ TEM
dealloying
X-ray nano-tomography
in situ synchrotron

ABSTRACT

In situ monitoring of corrosion processes is important to fundamentally understand the kinetics and evolution of materials in harsh environments. A *quasi in situ* transmission electron microscopy technique was utilized to study microstructural and chemical evolution of a Ni-20Cr disc sample exposed to molten KCl-$MgCl_2$ salt for 60 s in consecutive 20 s iterations. *In situ* synchrotron X-ray nano-tomography was performed to characterize the morphological evolution of a Ni-20Cr microwire exposed to molten KCl-$MgCl_2$. Both techniques captured key corrosion events and revealed mechanisms at different time and length scales, potentially bringing greater insights and deeper understanding beyond conventional analysis.

1. Introduction

The molten salt reactor (MSR) is one of the most promising generation IV reactor technologies that is being increasingly studied and developed by many private and governmental entities worldwide. Molten salts can serve as either a coolant or a fuel in a variety of MSR designs [1]. The use of molten salts in MSRs has many advantages such as enhanced safety due to passive cooling and low-pressure operation, better nuclear waste management and increased fuel efficiency and utilization [2,3]. Molten salts also find applications as high-temperature heat transfer fluids (HTF) in concentrated solar power (CSP) plants and thermal energy storage (TES) systems due to their excellent thermophysical properties [4–6]. One major challenge of molten salts is their corrosivity towards structural materials under anticipated operational conditions [7–10]. At present, Ni-based alloys are most commonly used in applications as salt-facing materials. Understanding corrosion mechanisms of Ni-based alloys in molten salts is critical to widespread industrial applications of molten salt-based systems.

Localized corrosion attacks can depend on a variety of factors, such as the nature of the grain boundary (GB), presence of a second phase and its distribution, grain sizes and orientations, local stress or defect concentrations [8,11–13]. Many traditional *ex situ* characterization techniques are only used after a certain amount of corrosion time. This makes identification of initial corrosion attack sites very challenging. In addition, analyzing small areas using scanning electron microscopy (SEM) or obtaining tiny transmission electron microscopy (TEM) samples from a relatively large corroded specimen may not be representative of all corrosion events. Therefore, *in situ* monitoring of corrosion processes is crucial to understand the fundamentals of corrosion mechanisms.

* Corresponding authors.
** Corresponding author at: Department of Materials Science and Chemical Engineering, Stony Brook University, Stony Brook, NY 11794, USA.
E-mail addresses: kaustubh.bawane@inl.gov (K. Bawane), Karen.Chen-Wiegart@stonybrook.edu (Y.-c.K. Chen-Wiegart), lingfeng.he@inl.gov (L. He).

https://doi.org/10.1016/j.corsci.2021.109962
Received 4 August 2021; Received in revised form 15 November 2021; Accepted 16 November 2021
Available online 20 November 2021
0010-938X/© 2021 Elsevier Ltd. All rights reserved.

In situ monitoring of molten salt corrosion has been previously reported by using electrochemical noise studies [14,15], X-ray diffraction [16] or by measuring changes in magnetic susceptibility [17]. Recent *in situ* TEM study on molten salt corrosion of Ni-based alloys revealed corrosion kinetics using diffraction pattern analysis, however, couldn't give good visualization of microstructural evolution [18]. *In situ* microscopy analysis of molten salt corrosion is only a recent development in X-ray [19] and electron-based techniques [18], and the method development in both techniques remain an active research area. Moreover, correlating the direct visualization of microstructural changes during molten salt corrosion at different time and length scales remains unexplored. *In situ* imaging of corrosion processes using TEM and scanning TEM (STEM) along with observations of real-time changes in composition and oxidation states using energy dispersive X-ray spectroscopy (EDS) and electron energy loss spectroscopy (EELS) can provide very important insights into reaction pathways and degradation behavior during early stages of corrosion. However, such experiments can be very expensive and involve specialized sample holders and time-consuming specimen preparation routines [18,20–22]. Recently, the use of *quasi in situ* TEM experiments to study corrosion processes have gained increasing attention especially in the field of aqueous corrosion of structural alloys [23–32]. Such experiments involve the corrosion of TEM samples in *ex situ* conditions for multiple iterations while observing the evolution of the same feature with TEM, thus creating an *in situ* like effect. Zheng *et al.* [23] successfully used a *quasi in situ* TEM technique to understand pitting behavior in stainless steel originating from dissolution of MnS inclusions during corrosion in aqueous NaCl solution. Jin *et al.* [30] used *quasi in situ* TEM to prove preferential dissolution of a Mg_2Ca phase during corrosion of Mg-0.5Zn-0.2Ca in aqueous NaCl solution. This paper for the first time reports a *quasi in situ* TEM study of corrosion in a molten salt environment. The high spatial resolution of the TEM (~sub-angstroms) uniquely enables characterizing detailed phenomena associated with the early stages of the dealloying and corrosion processes, especially considering the complex chemical interactions at metal-salt interfaces.

Transmission X-ray microscopy (TXM) in a synchrotron is another useful technique that can be used to characterize molten salt corrosion, albeit at lower resolutions (~30 nm). Ronne *et al.* [33] used synchrotron X-ray nano-tomography with TXM to study the three-dimensional (3D) morphological evolution of pure Ni and model Ni-20Cr alloy systems exposed to a molten KCl-$MgCl_2$ salt mixture at 800 °C with a multimodal, multi-scale imaging approach, combining synchrotron TXM nano-tomography with TEM analysis to obtain complementary information. A recently developed compact heater system has allowed direct visualization and quantification of molten salt corrosion damage in alloy microwire samples in real-time using *in situ* synchrotron X-ray nano-tomography [34]. More recently Liu *et al.* [19] conducted *operando* synchrotron X-ray nano-tomography using TXM to directly visualize, in 3D, the progression of molten salt corrosion of a Ni-20Cr alloy under elevated temperature at 700 °C. The results showed formation of an interconnected, so-called 'bicontinuous', pore/ligament network in Ni-20Cr, which was attributed to a percolation dealloying mechanism, namely leaching of Cr into the molten salt while Ni atoms rearrange *via* surface diffusion, coupled with an impurity-driven corrosion mechanism. The ability to image larger sample sizes than can be measured in TEM at a decent spatial resolution (tens of nm) in 3D makes *in situ* X-ray nano-tomography an ideal tool to characterize later stages of molten salt corrosion and is highly complementary to the *quasi in situ* TEM technique.

In this work, we demonstrate a time-resolved imaging using electron and X-ray based techniques at different length scales (~30 nm to sub-angstrom) to study molten salt corrosion, where *quasi in situ* TEM and *in situ* X-ray nano-tomography techniques were combined as a holistic approach to understand time-dependent microstructural, microchemical and morphological evolution. A model system of Ni-20Cr alloy reacted in a molten 68:32 mol% KCl-$MgCl_2$ salt mixture at 500 °C was directly visualized by both techniques during corrosion. As these two techniques operate at different time and length scales, the complementary nature of these two techniques enables each imaging method to provide unique information and together effectively capture key events to explain fundamental mechanisms at the interfaces in both the early and later stages of molten salt corrosion.

2. Materials and methods

2.1. Quasi in situ TEM for molten salt corrosion

As-rolled thin foil (thickness of ~250 μm) of Ni-20Cr model alloy was obtained from Goodfellow, USA. A 3 mm disc was punched from the foil using a Gatan disc punch system. The disc was polished down to 80 μm thickness using a series of SiC grit paper in the following order: 600, 800, and 1200. The TEM sample was prepared by thinning the Ni-20Cr disc using precision ion polishing system (Gatan PIPS-II) at the Center for Advanced Energy Studies (CAES). Argon ion milling was continued until a perforation appeared at the center of the disc using ion energies ranging from 4 keV to 0.5 keV. Final polishing at a low energy (0.5 keV) was performed to limit ion milling damage. Microstructural characterization was performed on the disc using a Thermo Scientific Titan TEM operated at 200 kV and the instrument was equipped with a Super-X EDS system at the Irradiated Materials Characterization Laboratory (IMCL) facility of Idaho National Laboratory (INL).

Fig. 1a shows the experimental setup for *quasi in situ* corrosion. A rolled Ni foil (thickness ~125 μm) was folded in the middle to hold the TEM disc sample. A small hole (diameter ~1.5 mm) was punched in Ni-foil holder near the fold to expose the TEM disc sample from both sides. The KCl-$MgCl_2$ eutectic salt mixture (32 mol.% $MgCl_2$-68 mol.% KCl) was prepared at Oak Ridge National Laboratory (ORNL) and shipped to INL for the corrosion test. The $MgCl_2$ salt was purified *via* fractional distillation from commercial anhydrous salt at 925 °C under 1×10^{-3} torr to remove contaminations including hexahydrate or MgO, following a procedure detailed in prior publications [19,33,35]. The KCl-$MgCl_2$ eutectic mixture was prepared by fusing the distilled $MgCl_2$ with anhydrous KCl procured from Alfa Aesar (99.998%, Lot N11F052) in the required proportions. For the corrosion tests at INL, a small top-loading furnace (Kerr Auto Electro-Melt Furnace Series 1258) housed inside an argon atmosphere glovebox (mBraun MB200B series) was used. The KCl-$MgCl_2$ mixture was melted at 500 °C in a glassy carbon crucible (GAZ 5, 50 mL Sigradur cylindrical crucible, HTW Germany). The crucible was cleaned with HPLC grade isopropanol (99.9% purity, Sigma-Aldrich) prior to use and baked at 700 °C under Ar for 4 h to remove any residual moisture and organic compounds adsorbed on the surface. The Ni-20Cr TEM disc sample secured in the Ni-foil holder was exposed to molten KCl-$MgCl_2$ salt for 20 s at a time, for a total of 3 repetitions. After each molten-salt bath treatment, the Ni-20Cr TEM disc along with the sample holder was cooled inside the glovebox for 30 min. It was then transferred out from the glovebox and the TEM disc was carefully removed from the Ni-foil holder for cleaning and removal of residual salts. The TEM disc was cleaned using glycerol (Equate 99.5% anhydrous, USP grade) in an ultrasonic bath for 30 s, followed by ethanol (Pharmco, 200 proof, absolute anhydrous, ACS/USP grade). The corrosion-induced microstructural changes in the treated, cleaned Ni-20Cr disc sample were then studied using the Thermo Scientific Titan Themis 200 TEM equipped with a Super-X EDS detection system at IMCL. This entire procedure was repeated for two more iterations of 20 s each (*i.e.,* total 40 s and 60 s of corrosion, respectively). TEM analysis was performed at the same disc locations after each exposure-clean iteration to observe the continuous evolution of molten salt corrosion damage *via* this *quasi in situ* TEM approach.

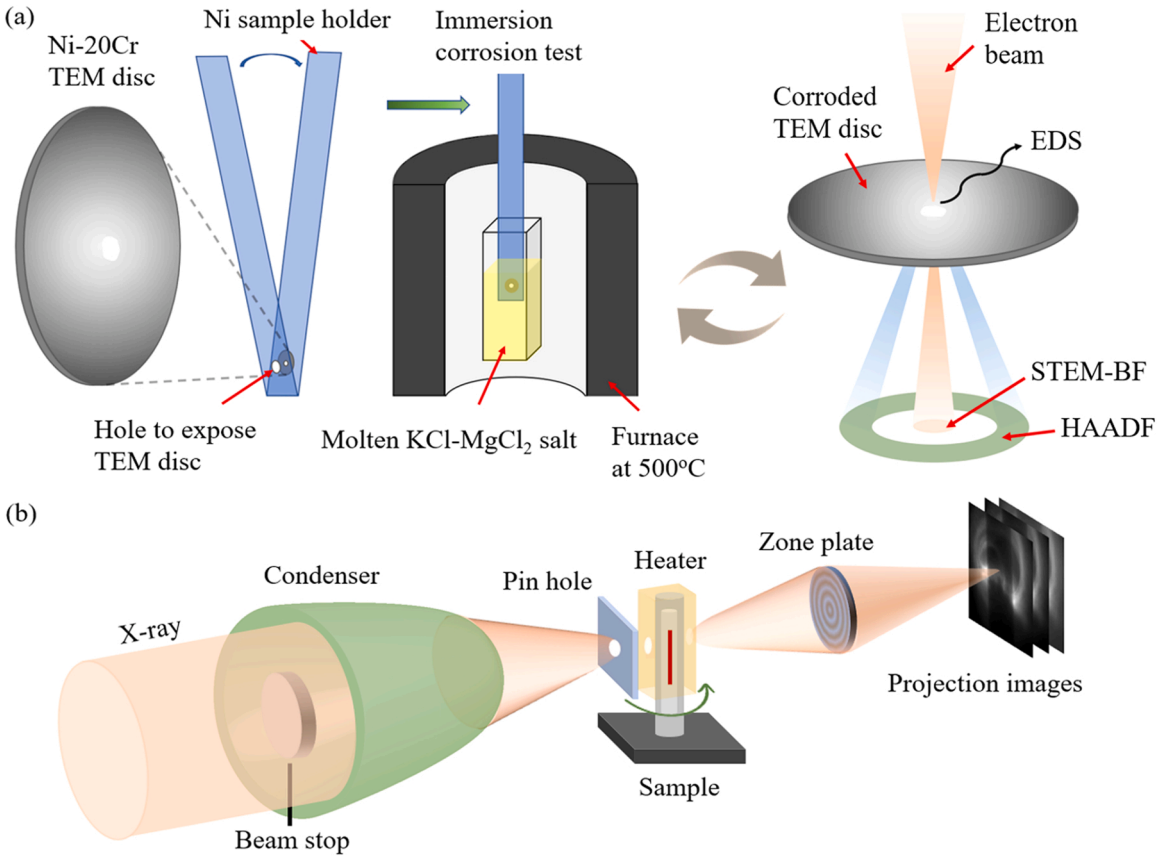

Fig. 1. Experimental setup for (a) *quasi in situ* molten salt corrosion of TEM sample, (b) *in situ* X-ray nano-tomography experiment setup for observing the 3D morphology evolution of Ni-20Cr in molten KCl-$MgCl_2$ at 500 °C.

2.2. *In situ* 3D X-ray nano-tomography in synchrotron during molten salt corrosion

A 20 μm as-drawn Ni-20Cr wire (80 wt% Ni and 20 wt% Cr, 99.5% pure, Goodfellow, USA-NI055105) was used to perform the *in situ* synchrotron experiment. The wire was put into an open-ended quartz capillary (0.1 mm outer diameter, Charles Supper). The wire-capillary sample assembly was baked out in a box furnace (CASCADE TEK, 120 °C) overnight to remove adsorbed surface moisture and transferred into an argon-filled glovebox immediately. The KCl was purchased as the 99.999% Suprapur reagent grade, opened and stored in the glovebox. In the glovebox, the purified KCl-$MgCl_2$ (50–50 mol.%) was melted in a quartz boat to ~ 550 °C. The molten salt was then drawn into the wire-capillary sample with a syringe, which is attached to the funnel side of the capillary. The molten salt was quickly solidified in the wire-containing capillary. Subsequently, the wire-capillary-salt sample was inserted into a larger quartz capillary with an outer diameter of 1.0 mm. The funnel side of the larger capillary was first temporarily sealed with epoxy and cured overnight inside the glovebox. The epoxy sealed sample was taken out and flame-sealed using a miniature benchtop hydrogen torch (Rio Grande). This methodology was developed and published in our prior work [19].

The *in situ* X-ray nano-tomography was conducted at the Full-field X-ray Imaging beamline (FXI, 18-ID) [36,37] at National Synchrotron Light Source II (NSLS-II) of Brookhaven National Laboratory. A miniature furnace was previously developed for the FXI beamline, as described in our prior work (Fig. 1. b) [34]. After calibrating the temperature, the furnace was heated to 500 °C with a ramp rate of 25 °C/min. Once the furnace reached the target temperature, 3D tomographic scans were then collected continuously. The incident X-ray energy was set to 8.33 keV to ensure an optimized imaging contrast. The field of view was 51.2 × 43.2 μm^2 with a pixel size of 40.0 nm. Each projection was collected with 50 ms exposure time, and a full tomographic measurement of 180° took ~2 or 3 min. Tomographic reconstructions were conducted using a python package Tomopy [38,39]. The Dragonfly (2020.1, Object Research Systems Inc) and Avizo (Thermo Fisher Scientific, v9.3) software were used to visualize the 3D reconstructed volumes.

3. Results and discussion

3.1. Tracking the early stages of molten salt corrosion using quasi in situ TEM

Molten salt corrosion-induced microstructural changes were tracked at four different locations (I-IV) of the Ni-20Cr TEM sample. These locations were selected randomly after the first iteration of corrosion and were tracked over subsequent iterations. Fig. 2a-c show STEM bright-field (STEM-BF) images of Location I after three iterations of molten salt corrosion, namely, 20, 40, and 60 s, respectively. Molten salt corrosion caused the formation and subsequent growth of cracks in the Ni-20Cr TEM sample as shown in Fig. 2a-c. The extent of corrosion damage was measured in terms of crack width at the edge and crack length. Molten salt corrosion for 20 s formed a relatively small crack 0.2 μm wide and 1.5 μm long as shown in Fig. 2a. After the second corrosion iteration (*i.e.,* 40 s), the crack width increased from 0.2 μm to 1 μm, and the crack length increased from 1.5 μm to 3.8 μm as shown in Fig. 2a and b. The crack that formed after 20 s corrosion at Zone 1 continued to broaden after 40 s, as shown in Fig. 2a and b. It should be noted that a narrow region of the crack in Zone 2 after the second iteration (40 s) indicates propagation of corrosion damage, leading to an increase in the overall crack length (see Fig. 2b). Fig. 2c shows the

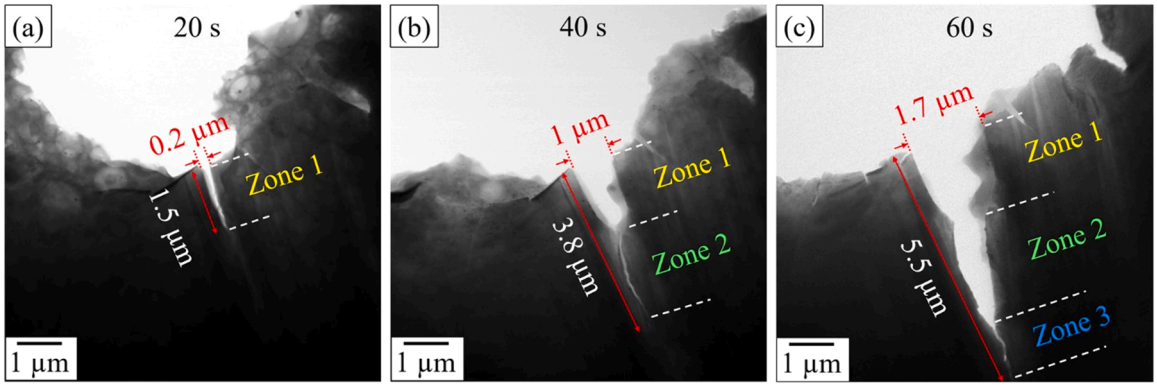

Fig. 2. STEM-BF images of the Ni-20Cr TEM sample (Location I) after corrosion in molten KCl-$MgCl_2$ at 500 °C for (a) 20 s, (b) 40 s, and (c) 60 s.

microstructure after the third iteration of corrosion (60 s). Both the crack width and length increased significantly to 1.7 µm and 5.5 µm, respectively, as shown in Fig. 2c. Corrosion propagation followed a similar pathway in the second iteration (40 s). The crack continued to broaden in Zone 1 and Zone 2, followed by a narrow, extended region at Zone 3 as shown Fig. 2c.

Selected area electron diffraction (SAED) pattern analysis in TEM was performed by choosing regions close to and on either side of the cracks shown in Location I, as shown in Fig. 3. The SAEDs (Fig. 3b-f) showed that among the four cracks analyzed, three were intergranular (marked with black solid arrows and numbers 1–3 in Fig. 3a) and one was intragranular (marked with a blue dashed arrow and number 4 in Fig. 3a). The intergranular crack denoted by number 2 is the same one tracked with corrosion time in Fig. 2. It should be noted that the intragranular crack was small as compared to the intergranular cracks (see Fig. 3a). This observation supports the assertion that GBs are the most preferred attack sites at early stages of molten salt corrosion in this system. The dotted red rectangle in Fig. 3a points to a region where thinning along the GBs likely occurred, just before the formation of cracks. Therefore, the formation of cracks can be attributed to preferential material removal along GBs from both surfaces (top and bottom) of the TEM disc sample because of molten salt corrosion. This means that molten salt corrosion of bulk sample will result in the formation of grooves along the GBs rather than the cracks due to attack only on one surface.

Fig. 4a and b show the microstructural evolution of Location II of the Ni-20Cr TEM sample after the first two iterations of *quasi in situ* corrosion (20 s and 40 s). The microstructure of Location II shows the formation of cracks at various locations after the first corrosion iteration (see Fig. 4a). The formation of a new crack (indicated by the solid red arrow in Fig. 4b) can be observed after the second corrosion iteration (40 s). This means that the corrosion process also propagates by new localized attacks to form cracks, along with growth of existing cracks. Similar to our observations at Location I, the broadening of existing cracks is evident in Fig. 4 (see dotted yellow circles). The corrosion attack is not limited to the formation of cracks but also the dissolution of edges of the TEM disc sample at locations indicated with green dotted arrows in Fig. 4a and b. After 60 s corrosion, most features in this location (II) were fully dissolved and therefore not included in Fig. 4.

High magnification STEM-BF images in Fig. 5 focus on a crack tip (Location III) to understand the corrosion propagation mechanisms. After 20 s corrosion, the microstructure shows that a part of the Ni-20Cr alloy near the crack tip denoted by a yellow arrow (see Fig. 5) remains undissolved, while corrosion and salt penetration occur around it. The

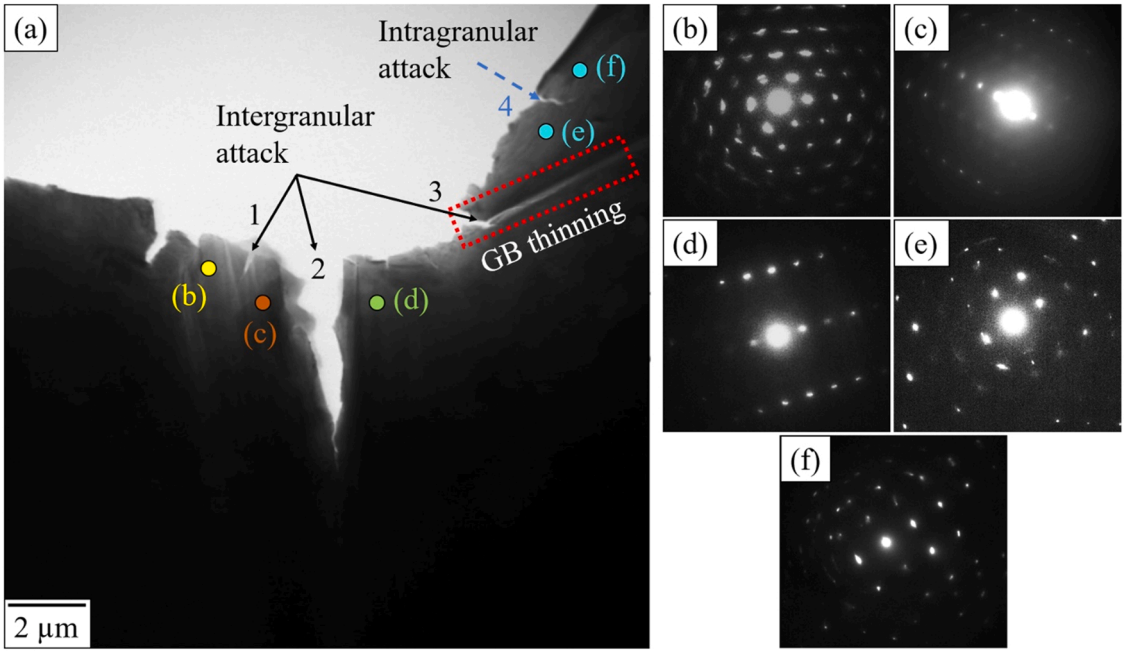

Fig. 3. STEM-BF image (a) and corresponding SAED patterns (b-f) at different locations in Ni-20Cr TEM sample (Location I) after corrosion in molten KCl-$MgCl_2$ at 500 °C for 60 s. (For interpretation of the references to colour in this figure, the reader is referred to the web version of this article.)

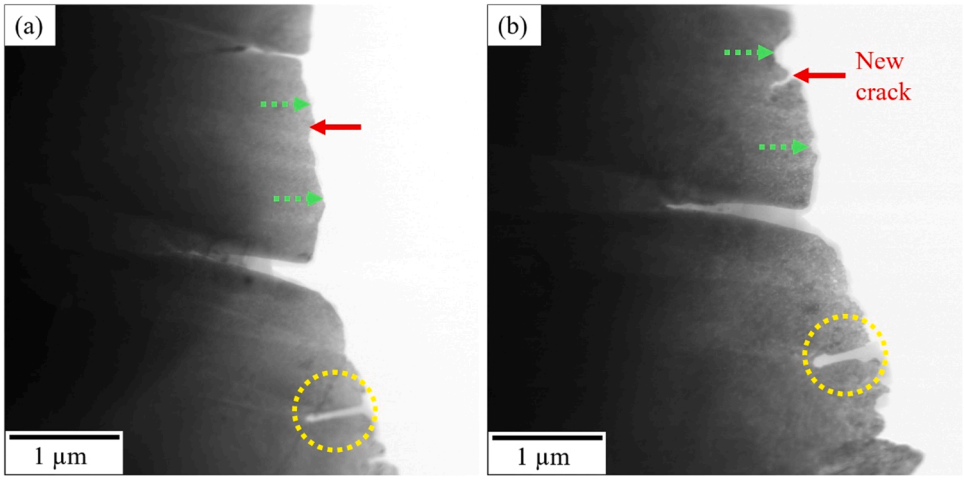

Fig. 4. STEM-BF images of Ni-20Cr TEM sample (Location II) after corrosion in molten KCl-$MgCl_2$ at 500 °C for (a) 20 s and (b) 40 s. (For interpretation of the references to colour in this figure, the reader is referred to the web version of this article.)

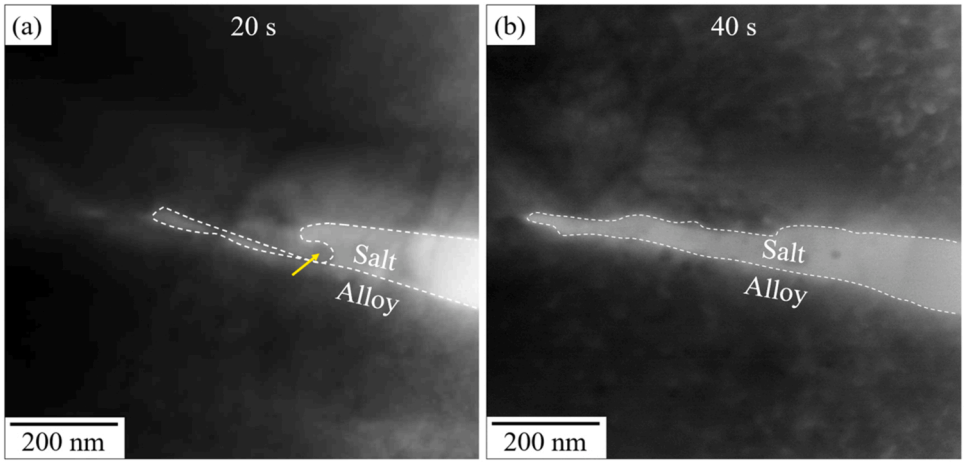

Fig. 5. STEM-BF images of Ni-20Cr TEM sample (Location III) after corrosion in molten KCl-$MgCl_2$ at 500 °C for (a) 20 s and (b) 40 s.

white dashed line tracing the salt/alloy interface illustrates this phenomenon clearly. Fig. 5b confirms that the second iteration of corrosion (40 s) dissolves this remaining Ni-20Cr alloy part to form a wider crack tip as compared to 20 s corrosion (see Fig. 5a). The morphology of the undissolved Ni-20Cr alloy part after 20 s corrosion (Fig. 5a) and its subsequent dissolution during the second iteration of corrosion provide an important visualization of the propagation of molten salt corrosion along the cracks.

Fig. 6 shows a STEM-BF image (Fig. 6a) and its corresponding EDS line scan (Fig. 6b) and maps (Fig. 6c) of another crack feature (Location IV) after 20 s corrosion. As mentioned in Section 2.1, after corrosion, the TEM sample was sonicated in glycerol, followed by further cleaning using ethanol to remove residual KCl-$MgCl_2$ salt. However, some KCl-$MgCl_2$ salt remained in the narrow cracks. This is evident from the line scan in Fig. 6b, which shows enrichments of Cl, Mg, and K in the crack region. The line scan also shows a small amount of Ni and Cr in this residual salt region, indicating alloy dissolution during molten salt corrosion. The line scan direction is shown in the STEM-BF image in Fig. 6a. EDS mapping around the crack confirms the enrichment of Cl, Mg, and K as shown in Fig. 6c. The features denoted by solid white circles in Fig. 6a appear to be particles barely clinging on the tip and edges of the crack. This feature is very similar to the remaining Ni-20Cr alloy part observed in Location III in Fig. 5a. The EDS mapping in Fig. 6c shows that these particles are Ni-rich and Cr-depleted. This means that Cr preferentially dissolves in the salt, leaving behind Ni-rich particles attached to the cracks. The wider crack tip in Fig. 5b proves that these Ni-rich particles will eventually dissolve with additional corrosion time.

3.2. *Visualizing the later stages of molten salt corrosion using in situ X-ray nano-tomography*

The *in situ* synchrotron X-ray nano-tomography results are presented in Fig. 7. The 2D pseudo cross-sectional views along the transverse (XY plane, Fig. 7a) and longitudinal (YZ plane, Fig. 7b) directions show the morphological evolution of a Ni-20Cr microwire with increasing reaction time in molten KCl-$MgCl_2$ salt at 500 °C. The morphologies at the initial and final time points are shown in an enlarged view, for both the XY view (red rectangles) and ZY view (blue rectangles). The onset of the corrosion propagates rapidly, creating sharp features; these features in the early corrosion stage are consistent with grain boundary attack as seen in the TEM analysis, while the TEM provides higher resolution to resolve the details.*insitu*

The interesting phenomenon from the TXM analysis is that, with prolonged reaction time, the dissolution of Cr occurred at the salt/alloy interface, leading to the formation of voids. This evolution is better observed with the 3D volume rendering view of the region near the interface (green dashed rectangle in Fig. 7a), as shown in Fig. 8. The voids are shown in yellow in Fig. 8a. With increasing time, the voids, which are filled with molten salt, propagated from the salt/alloy interface into the center of the sample. At ~ 121.2 min, these pores can be

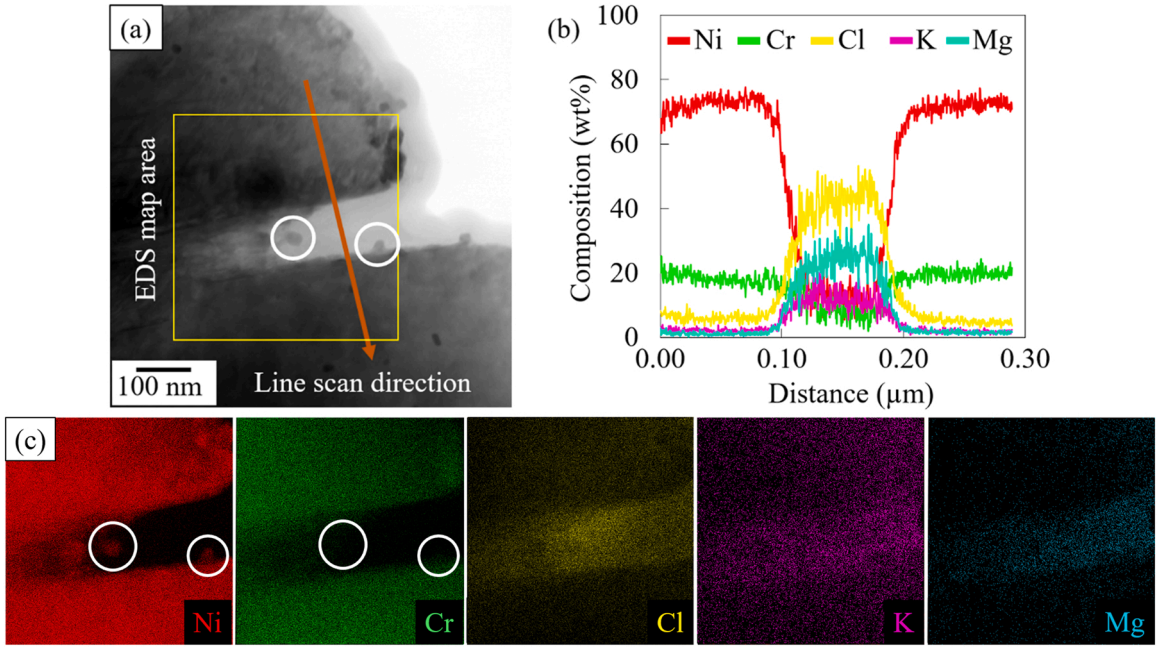

Fig. 6. STEM-EDS (a) mapping and (b) line scan and (c) EDS mapping of a Ni-20Cr TEM sample with residual salt (Location IV) after corrosion in molten KCl-$MgCl_2$ at 500 °C for 20 s.

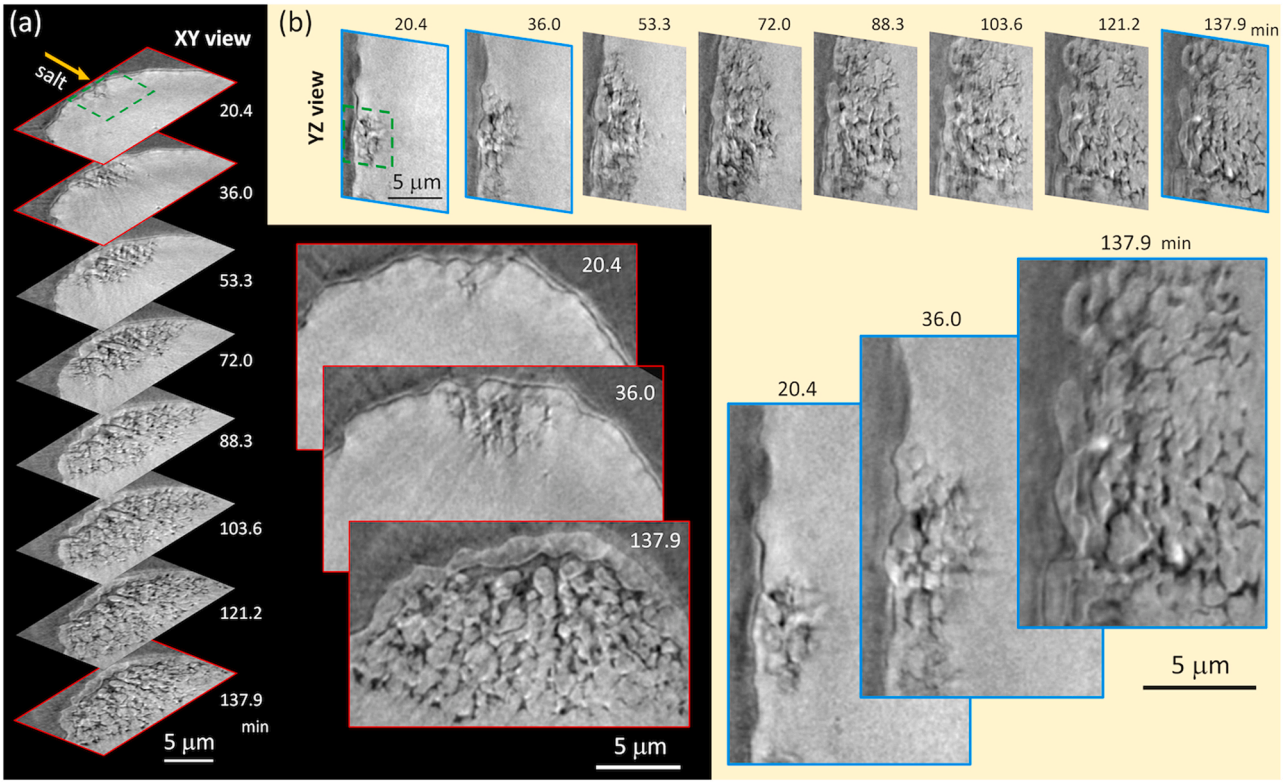

Fig. 7. 2D XY (a) and YZ (b) planes of the Ni-20Cr morphology evolution during the *insitu* heating experiment. The green frame highlighted the region for 3D visualization in Fig. 8. Enlarged views are shown for the initial and final time points, with further details shown in Fig. 8 as 3D views. (For interpretation of the references to colour in this figure, the reader is referred to the web version of this article.)

observed at the center of the wire. Subsequently, the size of the voids became larger with prolonged reaction time at 500 °C as shown in Fig. 8b. From ~106–138 min, the voids gradually grew larger. Noticeably, the initial voids remained elongated in shape, resembling the cracks observed in STEM. These elongated voids or connected long cracks then grew laterally, which indicates that the corrosion attacked into the grain as shown in the red arrow. Here, the interplay of several chemical reactions and transport mechanisms leads to the progression of the material's morphology, which is discussed in the next section.

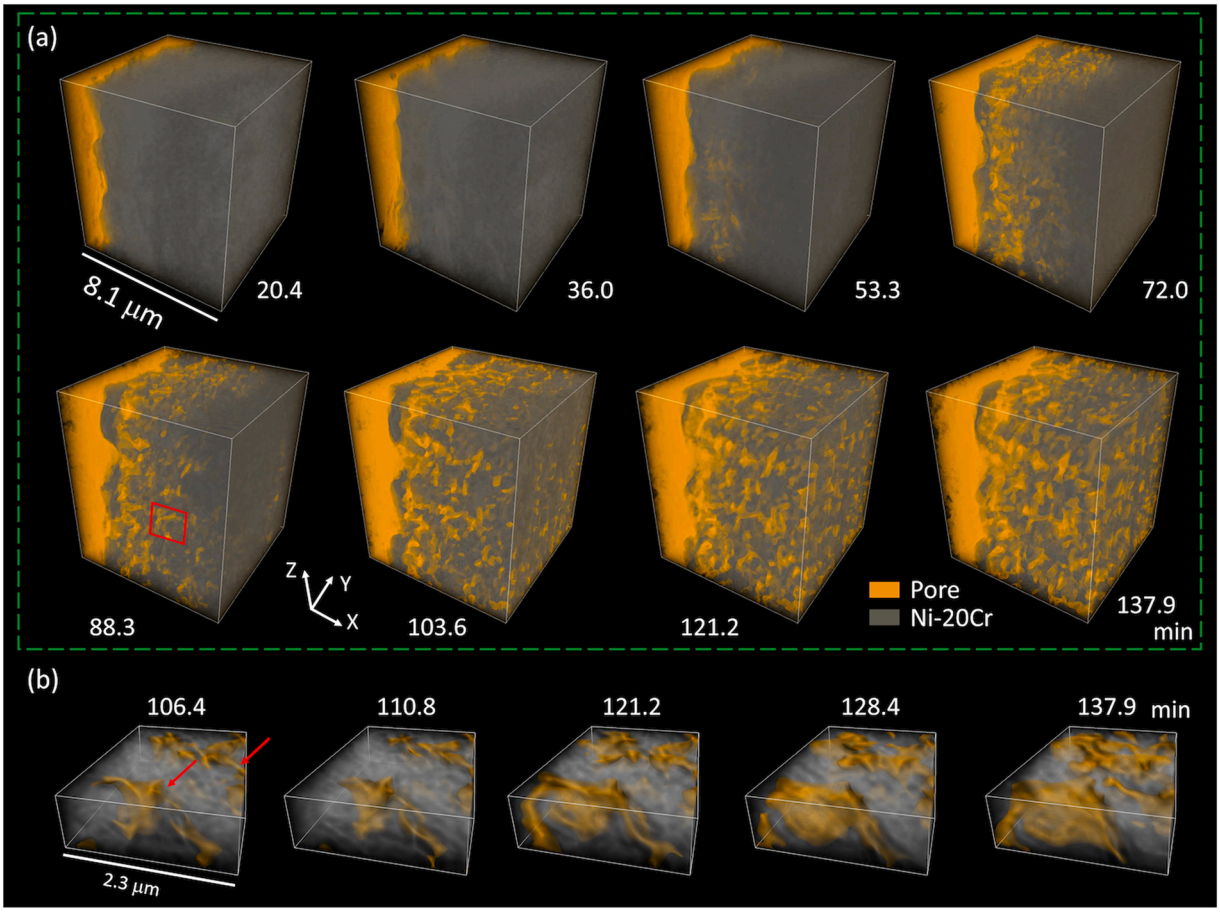

Fig. 8. 3D views of the selected region in Ni-20Cr showing pore propagation from the metal-salt interface to the center of the sample. (a) An overview of the 3D morphological evolution in the region near the interface as highlighted in Fig. 7 with green dashed rectangles. (b) A representative region (red rectangle from a) shows the growth of the pores into the grain after grain boundary corrosion as indicated by the red arrow. (For interpretation of the references to colour in this figure, the reader is referred to the web version of this article.)

3.3. *Fundamental understanding of corrosion mechanisms*

The *quasi in situ* TEM study provides valuable insights into mechanisms of various stages of molten salt corrosion and morphological evolution in the Ni-20Cr alloy. Fig. 9a shows a schematic representation of microstructure evolution as a function of corrosion time.

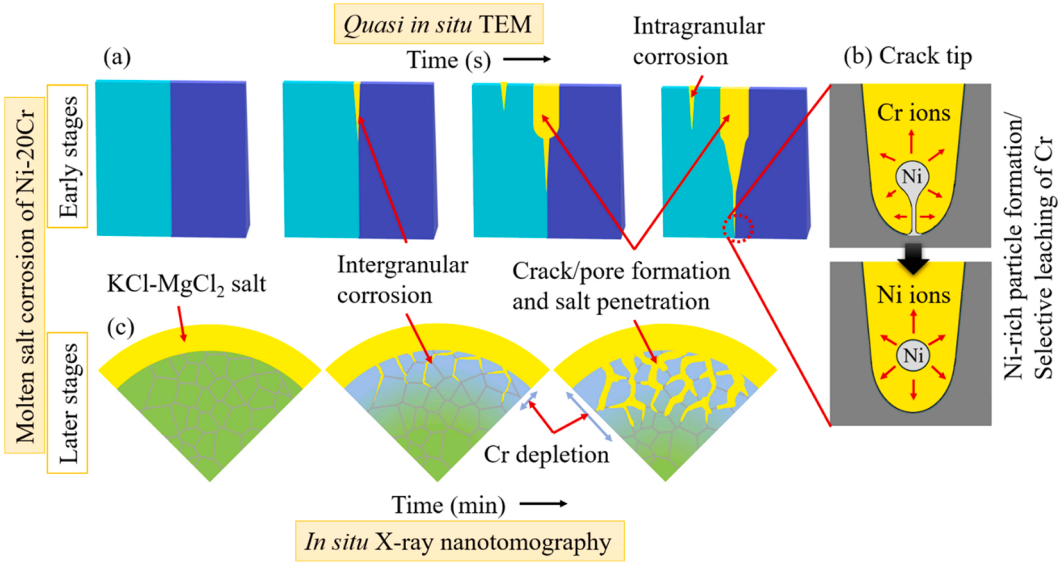

Fig. 9. Schematic representation of (a) corrosion at grain boundaries, (b) formation of Ni-rich particles in the molten salt during *quasi in situ* corrosion of Ni-20Cr TEM sample, (c) a schematic representation of the corrosion of the Ni-20Cr microwire during the *in situ* X-ray nano-tomography characterization.

Corrosion damage in the TEM sample mainly manifests as cracking, crack growth and broadening as shown in Fig. 9a. The cracking occurred because of localized material removal on both surfaces (top and bottom) of the TEM sample and the corrosion attack fronts on top and bottom surfaces along same GB met each other soon after corrosion due to the small thickness of the TEM disc sample. The STEM-BF image and SAEDs in Fig. 3 indicate that these cracks formed preferentially along the GBs. The GB thinning observed in Fig. 3 demonstrates preferential intergranular material removal. Intergranular attack during *ex situ* molten salt corrosion studies has been reported by several researchers over the years [8,40–45]. The material removal or leaching and intergranular corrosion in multicomponent alloys could be the result of selective dissolution of the least noble alloying element, in this case, Cr [8,9,33,41,43–51].

A continuous leaching process leading to crack and pore formation requires both chemical reactions and mass transport processes to take place. In a molten salt bath with a static, isothermal environment, the primary transport mechanism is solid-state diffusion of alloying elements towards the salt/alloy interface to react with the molten salt. The oxidation reactions of the alloy components (Ni and Cr) with molten salt leads to dissolution (Eqs. 1–3). It should be noted that oxidized Cr exists as either Cr^{2+} or Cr^{3+} (Eq. 2). Our previous work on EELS characterization of *ex situ* Ni-20Cr alloy corrosion revealed that dissolved Cr was primarily in the trivalent form Cr^{3+} [52]. The oxidation states of elements in a molten salt depend on multiple factors such as reaction thermodynamics and the presence of impurities such as oxygen, water, or other elements [47,53]. EELS characterization was not performed in this work due to the relatively large thickness of residual salt in the *quasi in situ* Ni-20Cr TEM sample.

$$Cr_{(alloy)} = Cr^{2+}_{(salt)} + 2e^- \quad (1)$$

$$Cr^{2+}_{(salt)} = Cr^{3+}_{(salt)} + e^- \quad (2)$$

$$Ni_{(alloy)} = Ni^{2+}_{(salt)} + 2e^- \quad (3)$$

It is well known that diffusion coefficients of alloying elements in GBs are often higher than in the lattice [47,54]. Chen *et al.* [54] reported GB diffusion coefficients of Cr to be a few orders of magnitude higher than its volume diffusion coefficients in various Ni-Cr-Fe alloys. The preferential intergranular attack can be attributed to faster diffusion of Cr in GBs as compared to the lattice of Ni-20Cr. The Cr diffusion and subsequent dissolution in the molten salt eventually creates voids along the GBs which are then filled with molten salt, leading to an advancing corrosion front (in this case, GB cracks) [9,12,13,33,47,55–57]. The salt penetration in the cracks is evident in the EDS line scan and the EDS map in Fig. 6 and illustrated in the schematic diagram in Fig. 9a. The selective Cr dissolution was successfully visualized using the *quasi in situ* TEM technique (Fig. 6). The Ni-rich/Cr-lean particle formation close to the salt/alloy interface (see Figs. 5 and 6) is not only evidence of preferential Cr dissolution but also provides direct visualization and insight on how corrosion fronts propagate during the early stages of molten salt corrosion for the first time. This Ni-rich/Cr-lean particle formation process is illustrated in the schematic diagram in Fig. 9b. Ni dissolution should follow Cr dissolution during the molten salt corrosion as shown in Figs. 5b and 9b. Although effects such as preferential attack on GBs and selective leaching of active elements like Cr are well known in the molten salt corrosion community, the reported results provide the first nanoscale observations of morphological and chemical changes associated with GB attack.

It is worth noting that along with intergranular cracks, some small intragranular cracks were also observed after molten salt corrosion as shown in Fig. 3. The intragranular cracking may depend on the surface or edge conditions of the TEM sample. It is well known that surface conditions such as roughness and impurities can act as corrosion initiation sites and have a profound impact on the severity of corrosion [58,59].

The broadening and growth of cracks are illustrated in Fig. 9a. With subsequent corrosion, it is possible that all intergranular and intragranular cracks intersect and connect to form a network such that small pieces of Ni-20Cr alloy can detach from the bulk. The cracks can eventually broaden and become larger than the grain size itself, which can obscure knowledge of the initial attack sites during molten salt corrosion. The *quasi in situ* TEM study effectively provides a detailed visualization of key events and corrosion processes during the early stages of molten salt corrosion which is not often possible with *ex situ* studies.

In conjunction, the *in situ* X-ray nano-tomography work here imaged 3D morphological evolution during molten salt corrosion in real-time toward the later stage of the reaction. As mentioned, the interplay of several chemical reactions and transport mechanisms (primarily diffusion, as explained) leads to the progression of the material's morphology. In addition to the GB corrosion mechanism, additional diffusion mechanisms may be considered for corrosion propagation into the grains during molten salt corrosion. Firstly, after the Cr preferentially reacted out along the GBs, the bulk diffusion of Cr or Ni could occur due to a concentration gradient in the Ni-20Cr alloy (*i.e.* the GBs are Cr depleted and Ni-rich). However, Zhou *et al.* indicated that bulk diffusion would be too slow to compensate for the formation of pores at 650 °C [60]. The temperature used in our current study was 500 °C which means that the bulk diffusion of Cr and Ni would be even slower to replenish the loss of Cr at the metal-salt interface resulting in a broadening of the intergranular pores into the grain.

Moreover, previous studies proposed a percolation dealloying mechanism in molten salt corrosion forming a bicontinuous porous structure at 800 °C [19,33]. Interestingly, no obvious bicontinuous porous structure formed in this study at 500 °C. This may be attributed to the complex chemical reactions and interfacial conditions in the molten salt corrosion environment. For instance, the solubility of $CrCl_3$ is ~10.9 mol.% in KCl-$MgCl_2$ (50–50 mol.%) at 800 °C [19]. The solubilities and diffusion rates of corrosion products at 500 °C in the molten salt would be lower than at 800 °C. A local accumulation of corrosion products may suppress the selective dissolution of Cr. On the other hand, the surface diffusion of Ni would be too slow at 500 °C to sustain a coarsening process, which is a pre-requisite to creating the porous structure. Snyder *et al.* suggested that without coarsening, the noble element could passivate the surface [61]. Because of the relatively low temperature, after the initial dissolution of Cr, Ni may passivate the grain surface from further corrosion into the grain. Further analysis and simulation are needed to quantify how different diffusion processes during molten salt corrosion influence the morphological evolution.

Quasi in situ TEM and *in situ* X-ray nano-tomography techniques proved to be complementary to each other. The major connection between the two techniques is that the formation of interconnected pores observed during the early stages of the *in situ* X-ray nano-tomography measurements can be explained by the *quasi in situ* TEM experiments, where nucleation and subsequent lengthening/broadening of cracks along grain boundaries and within grains can eventually cause the cracks to merge with each other. The cracks in the TEM sample can be perceived as 2D versions of the pores in the bulk sample. The subsequent *in situ* synchrotron X-ray nano-tomography gives 3D visualization of further evolution of interconnected pores. Due to very small length scales, localized nature of corrosion attacks and rapid growth of corrosion front from initial attack site, *ex situ* microstructural characterization is often not enough to understand key corrosion events and their evolution with time. The ability to observe microstructural and chemical evolution of an entire corroded area with time distinguishes this work from previously reported *ex situ* corrosion work. The combination of the two techniques provides a more complete picture of molten salt corrosion, starting from early-stage local corrosion phenomena in TEM to interconnected pore structure formation during prolonged corrosion time in TXM. In the future, these techniques can be used to study the effects of alloying elements, grain size/orientation, the presence of

fission products in the salt, irradiation (defects and segregation behavior), and stress (deformation) on molten salt corrosion. Some of this work is already underway in our Molten Salts for Extreme Environments (MSEE) Energy Frontier Research Center (EFRC). The time-dependent 2D (*quasi in situ* TEM) and 3D (*in situ* X-ray nano-tomography) microstructures obtained in this work can be a great resource to benchmark simulations predicting microstructural evolution during molten salt corrosion. Recently, Wang *et al.* [62] used cellular automata simulations to predict the corrosion of Ni alloys in molten chloride salt systems. The Yellowjacket program using MOOSE (Multiphysics Object Oriented Simulation Environment) framework at INL is also modeling molten salt corrosion behaviors with mesoscale phase field simulations [63,64].

4. Conclusion

Quasi in situ TEM and *in situ* X-ray nano-tomography work enabled direct observation of time-dependent evolution of molten salt corrosion at their respective time and length scales. *Quasi in situ* TEM work was successful in understanding mechanisms during early stages of molten salt corrosion and visualizing corrosion phenomena at the nanoscale. The *quasi in situ* TEM technique observed three major phenomena linked to molten salt corrosion: intergranular corrosion, advancing of the corrosion front, and preferential dealloying. *In situ* X-ray nano-tomography work was successful in understanding 3D microstructure and evolution of interconnected pore-salt networks in real-time. This work provides a basis to utilize this correlative approach to gain a fundamental understanding of molten salt corrosion involving more complex combinations of alloys and salts, and to aid in the design and development of new structural materials and methods to mitigate molten salt corrosion.

CRediT authorship contribution statement

Kaustubh Bawane: Investigation, Methodology, Writing – original draft preparation. **Xiaoyang Liu:** Investigation, Methodology, Writing – original draft preparation. **Ruchi Gakhar:** Investigation, Writing – review & editing. **Michael Woods:** Investigation. **Mingyuan Ge:** Investigation. **Xianghui Xiao:** Investigation. **Wah-Keat Lee:** Investigation. **Philip Halstenberg:** Investigation. **Sheng Dai:** Supervision, Funding acquisition. **Shannon Mahurin:** Supervision, Funding acquisition, Writing – review & editing. **Simon M. Pimblott:** Supervision, Funding acquisition, Project administration, Writing – review & editing. **James F. Wishart:** Supervision, Funding acquisition, Project administration, Writing – review & editing. **Yu-chen Karen Chen-Wiegart:** Conceptualization, Supervision, Funding acquisition, Writing – review & editing. **Lingfeng He:** Conceptualization, Supervision, Funding acquisition, Writing – review & editing.

Declaration of Competing Interest

The authors declare that they have no known competing financial interests or personal relationships that could have appeared to influence the work reported in this paper.

Data Availability

The raw/processed data required to reproduce these findings cannot be shared at this time as the data is part of ongoing study and will be shared on request.

Acknowledgments

This work was supported as part of the Molten Salts in Extreme Environments Energy Frontier Research Center, funded by the U.S. Department of Energy, Office of Science. Brookhaven National Laboratory, Idaho National Laboratory, and Oak Ridge National Laboratory are operated under DOE contracts DESC0012704, DE-AC07-05ID14517, and DEAC05-00OR22725, respectively. This research used resources and the Full Field X-ray Imaging (FXI, 18-ID) beamline of the National Synchrotron Light Source II, a U.S. Department of Energy (DOE) Office of Science User Facility operated for the DOE Office of Science by Brookhaven National Laboratory under Contract No. DE-SC0012704. The authors also acknowledge the U.S. Department of Energy, Office of Nuclear Energy under DOE Idaho Operations Office Contract DE-AC07-051D14517, for use of the resources as part of Nuclear Science User Facilities. The authors thank Yaqiao Wu, and Jeremy Burgener at the Center for Advanced Energy Studies, and Miles Cook, Jayson Bush, Jeffery Bailey at Idaho National Laboratory for their invaluable assistance. The authors acknowledge Dr. Kazuhiro Iwamatsu, Arthur Ronne, Lin-Chieh Yu and Bobby Layne for their assistance during the synchrotron sample preparation. We thank Cheng-Hung Lin for assisting on the tomographic data reconstruction. Chen-Wiegart group members are acknowledged for their participation in the FXI beamtime experiment: Karol Dyro, Dean Yen, Chonghang Zhao and Cheng-Hung Lin, Lin-Chieh Yu and Arthur Ronne.

References

[1] J. Serp, M. Allibert, O. Beneš, S. Delpech, O. Feynberg, V. Ghetta, D. Heuer, D. Holcomb, V. Ignatiev, J.L. Kloosterman, L. Luzzi, E. Merle-Lucotte, J. Uhlíř, R. Yoshioka, D. Zhimin, The molten salt reactor (MSR) in generation IV: overview and perspectives, Prog. Nucl. Energy 77 (2014) 308–319.
[2] C.W. Forsberg , Molten-salt-reactortechnology gaps, International Congress on the Advances in Nuclear PowerPlants, Reno, NV, USA, 2006.
[3] D. LeBlanc, Molten salt reactors: a new beginning for an old idea, Nucl. Eng. Des. 240 (6) (2010) 1644–1656.
[4] W. Ding, A. Bonk, T. Bauer, Molten chloride salts for next generation CSP plants: Selection of promising chloride salts & study on corrosion of alloys in molten chloride salts, AIP Conference Proceedings 2126(1) 2019 200014.
[5] A.G. Fernández, L.F. Cabeza, Corrosion evaluation of eutectic chloride molten salt for new generation of CSP plants. Part 2: Materials screening performance, J. Energy Storage 29 (2020), 101381.
[6] J.M. Kurley, P.W. Halstenberg, A. McAlister, S. Raiman, S. Dai, R.T. Mayes, Enabling chloride salts for thermal energy storage: implications of salt purity, RSC Adv. 9 (44) (2019) 25602–25608.
[7] V. Ignatiev, A. Surenkov, 5 - Corrosion phenomena induced by molten salts in Generation IV nuclear reactors, in: P. Yvon (Ed.), Structural Materials for Generation IV Nuclear Reactors, Woodhead Publishing, 2017, pp. 153–189.
[8] S. Guo, J. Zhang, W. Wu, W. Zhou, Corrosion in the molten fluoride and chloride salts and materials development for nuclear applications, Prog. Mater. Sci. 97 (2018) 448–487.
[9] K. Sridharan, T.R. Allen, 12 - Corrosion in molten salts, in: F. Lantelme, H. Groult (Eds.), Molten Salts Chemistry, Elsevier, Oxford, 2013, pp. 241–267.
[10] S.S. Raiman, S. Lee, Aggregation and data analysis of corrosion studies in molten chloride and fluoride salts, J. Nucl. Mater. 511 (2018) 523–535.
[11] G. Zheng, L. He, D. Carpenter, K. Sridharan, Corrosion-induced microstructural developments in 316 stainless steel during exposure to molten Li2BeF4(FLiBe) salt, J. Nucl. Mater. 482 (2016) 147–155.
[12] W. Zhou, Y. Yang, G. Zheng, K.B. Woller, P.W. Stahle, A.M. Minor, M.P. Short, Proton irradiation-decelerated intergranular corrosion of Ni-Cr alloys in molten salt, Nat. Commun. 11 (1) (2020) 3430.
[13] Z. Zhu, H. Huang, G. Lei, Y. Wu, C. Ren, A. Liu, Z. Zhu, Synergistic effect of irradiation and molten salt corrosion: acceleration or deceleration? Corros. Sci. 185 (2021), 109434.
[14] J.L. Dawson, Electrochemical noise measurement: the definitive in-situ technique for corrosion applications? in: J.R. Kearns, J.R. Scully, P.R. Roberge, D.L. Reichert, J.L. Dawson (Eds.) ASTM International, West Conshohocken, PA, 1996, pp. 3–35.
[15] G. Gao, F.H. Stott, J.L. Dawson, D.M. Farrell, Electrochemical monitoring of high-temperature molten-salt corrosion, Oxid. Met. 33 (1) (1990) 79–94.
[16] Q. Lei, X. Zhang, M. Gao, W. Wen, Y. Jia, H. Liu, Y. Li, J. Liu, X. Zhou, Inconel 617 corrosion in FLiNaK molten salts: an in situ X-ray diffraction study, Corros. Sci. 182 (2021), 109289.
[17] N.D.B. Ezell, R. Kisner, N. Russell, F.K. Reed, P. Champlin, J. Keiser, A. Martin, D. Holcomb, Development of a Corrosion Monitoring System for Molten Salt Reactors (ORNL/TM-2019/1273, Oak Ridge National Laboratory, 2019.
[18] P. Pragnya, D. Gall, R. Hull, In Situ transmission electron microscopy of high-temperature Inconel-625 corrosion by molten chloride salts, J. Electrochem. Soc. 168 (5) (2021), 051507.
[19] X. Liu, A. Ronne, L.-C. Yu, Y. Liu, M. Ge, C.-H. Lin, B. Layne, P. Halstenberg, D. S. Maltsev, A. Ivanov, S. Antonelli, S. Dai, W.-K. Lee, S.M. Mahurin, A.I. Frenkel, J. F. Wishart, X. Xiao, Y.-c.K. Chen-Wiegart, Formation of three-dimensional bicontinuous structures via molten salt dealloying studied in real-time by in situ synchrotron X-ray nano-tomography, Nat. Commun. 12 (2021), 3441.

[20] J.W. Key, S. Zhu, C.M. Rouleau, R.R. Unocic, Y. Xie, J. Kacher, Investigating local oxidation processes in Fe thin films in a water vapor environment by in situ liquid cell TEM, Ultramicroscopy 209 (2020), 112842.
[21] K.A. Unocic, F.S. Walden, N.L. Marthe, A.K. Datye, W.C. Bigelow, L.F. Allard, Introducing and controlling water vapor in closed-cell in situ electron microscopy gas reactions, Microsc. Microanal. 26 (2) (2020) 229–239.
[22] L. Liu , J. Zhang , K. Ramik , Development of in-situ corrosion kinetics and salt property measurements SETO CSP Program Summit 2019.
[23] S.J. Zheng, Y.J. Wang, B. Zhang, Y.L. Zhu, C. Liu, P. Hu, X.L. Ma, Identification of MnCr2O4 nano-octahedron in catalysing pitting corrosion of austenitic stainless steels, Acta Mater. 58 (15) (2010) 5070–5085.
[24] S.R.K. Malladi, F.D. Tichelaar, Q. Xu, M.Y. Wu, H. Terryn, J.M.C. Mol, F. Hannour, H.W. Zandbergen, Quasi in situ analytical TEM to investigate electrochemically induced microstructural changes in alloys: AA2024-T3 as an example, Corros. Sci. 69 (2013) 221–225.
[25] S.R.K. Malladi, Q. Xu, F.D. Tichelaar, H.W. Zandbergen, F. Hannour, J.M.C. Mol, H. Terryn, Early stages during localized corrosion of AA2024 TEM specimens in chloride environment, Surf. Interface Anal. 45 (10) (2013) 1619–1625.
[26] B. Zhang, J. Wang, B. Wu, Y.T. Zhou, X.L. Ma, Quasi-in-situ ex-polarized TEM observation on dissolution of MnS inclusions and metastable pitting of austenitic stainless steel, Corros. Sci. 100 (2015) 295–305.
[27] F.A. Almuaili, S.A. McDonald, P.J. Withers, D.L. Engelberg, Application of a quasi in situ experimental approach to estimate 3-D pitting corrosion kinetics in stainless steel, J. Electrochem. Soc. 163 (13) (2016) C745–C751.
[28] S.K. Kairy, P.A. Rometsch, C.H.J. Davies, N. Birbilis, On the electrochemical and quasi in situ corrosion response of the Q-Phase (AlxCuyMgzSiw) intermetallic particle in 6xxx series aluminum alloys, Corrosion 73 (1) (2016) 87–99.
[29] Y. Zhang, P. Gore, W. Rong, Y. Wu, Y. Yan, R. Zhang, L. Peng, J.-F. Nie, N. Birbilis, Quasi-in-situ STEM-EDS insight into the role of Ag in the corrosion behaviour of Mg-Gd-Zr alloys, Corros. Sci. 136 (2018) 106–118.
[30] Y. Jin, C. Blawert, F. Feyerabend, J. Bohlen, M. Silva Campos, S. Gavras, B. Wiese, D. Mei, M. Deng, H. Yang, R. Willumeit-Römer, Time-sequential corrosion behaviour observation of micro-alloyed Mg-0.5Zn-0.2Ca alloy via a quasi-in situ approach, Corros. Sci. 158 (2019), 108096.
[31] S.K. Kairy, N. Birbilis, Clarifying the role of Mg2Si and Si in localized corrosion of aluminum alloys by quasi in situ transmission electron microscopy, Corrosion 76 (5) (2020) 464–475.
[32] Y.T. Zhou, Y.N. Zan, Q.Z. Wang, B.L. Xiao, Z.Y. Ma, X.L. Ma, Atomic-scale quasi in-situ TEM observation on the redistribution of alloying element Cu in a B4C/Al composite at the initial stage of corrosion, Corros. Sci. 174 (2020), 108808.
[33] A. Ronne, L. He, D. Dolzhnikov, Y. Xie, M. Ge, P. Halstenberg, Y. Wang, B. T. Manard, X. Xiao, W.K. Lee, K. Sasaki, S. Dai, S.M. Mahurin, Y.K. Chen-Wiegart, Revealing 3D morphological and chemical evolution mechanisms of metals in molten salt by multimodal microscopy, ACS Appl. Mater. Interfaces 12 (15) (2020) 17321–17333.
[34] S. Antonelli, A. Ronne, I. Han, M. Ge, B. Layne, A.J. Shahani, K. Iwamatsu, J. F. Wishart, S.L. Hulbert, W.-K. Lee, Y.-ck. Chen-Wiegart, X. Xiao, Versatile compact heater design for in situ nano-tomography by transmission X-ray microscopy, J. Synchrotron Radiat. 27 (3) (2020) 746–752.
[35] F. Wu, S. Roy, A.S. Ivanov, S.K. Gill, M. Topsakal, E. Dooryhee, M. Abeykoon, G. Kwon, L.C. Gallington, P. Halstenberg, B. Layne, Y. Ishii, S.M. Mahurin, S. Dai, V.S. Bryantsev, C.J. Margulis, Elucidating ionic correlations beyond simple charge alternation in molten MgCl2–KCl Mixtures, J. Phys. Chem. Lett. 10 (24) (2019) 7603–7610.
[36] Full field X-ray imaging (FXI) ⟨https://www.bnl.gov/nsls2/beamlines/beamline.php?r=18-ID⟩.
[37] M. Ge, D.S. Coburn, E. Nazaretski, W. Xu, K. Gofron, H. Xu, Z. Yin, W.-K. Lee, One-minute nano-tomography using hard X-ray full-field transmission microscope, Appl. Phys. Lett. 113 (8) (2018), 083109.
[38] D. Gursoy, F. De Carlo, X.H. Xiao, C. Jacobsen, TomoPy: a framework for the analysis of synchrotron tomographic data, J. Synchrotron Radiat. 21 (2014) 1188–1193.
[39] B.A. Dowd, G.H. Campbell, R.B. Marr, V. Nagarkar, S. Tipnis, L. Axe, D.P. Siddons, Developments in synchrotron x-ray computed microtomography at the National Synchrotron Light Source, Conference on Developments in X-Ray Tomography II, Denver, Co, 1999, pp. 224–236.
[40] Corrosion in Molten Salts, High Temperature Corrosion (2019) 296–324.
[41] J.C. Gomez-Vidal, R. Tirawat, Corrosion of alloys in a chloride molten salt (NaCl-LiCl) for solar thermal technologies, Sol. Energy Mater. Sol. Cells 157 (2016) 234–244.
[42] L. Guo, Q. Liu, H. Yin, T.J. Pan, Z. Tang, Excellent corrosion resistance of 316 stainless steel in purified NaCl-MgCl2 eutectic salt at high temperature, Corros. Sci. 166 (2020), 108473.
[43] W. Wang, B. Guan, X. Li, J. Lu, J. Ding, Corrosion behavior and mechanism of austenitic stainless steels in a new quaternary molten salt for concentrating solar power, Sol. Energy Mater. Sol. Cells 194 (2019) 36–46.
[44] H. Sun, J. Wang, Z. Li, P. Zhang, X. Su, Corrosion behavior of 316SS and Ni-based alloys in a ternary NaCl-KCl-MgCl2 molten salt, Sol. Energy 171 (2018) 320–329.
[45] H. Sun, P. Zhang, J. Wang, Effects of alloying elements on the corrosion behavior of Ni-based alloys in molten NaCl-KCl-MgCl2 salt at different temperatures, Corros. Sci. 143 (2018) 187–199.
[46] L.C. Olson, J.W. Ambrosek, K. Sridharan, M.H. Anderson, T.R. Allen, Materials corrosion in molten LiF–NaF–KF salt, J. Fluor. Chem. 130 (1) (2009) 67–73.
[47] S.K. Gill, J. Sure, Y.C. Wang, B. Layne, L.F. He, S. Mahurin, J.F. Wishart, K. Sasaki, Investigating corrosion behavior of Ni and Ni-20Cr in molten ZnCl2, Corros. Sci. 179 (2021).
[48] J.W. Koger, Alloy compatibility with LiF–BeF_2 salts containing ThF_4 and UF_4, United States, 1972.
[49] J.H. DeVan, Effect of alloying additions on corrosion behavior of nickel-molybdenum alloys in fused fluoride mixtures, United States, 1969.
[50] W.R. Grimes, Molten-salt reactor chemistry, Nucl. Appl. Technol. 8 (2) (1970) 137–155.
[51] W. Ding, J. Gomez-Vidal, A. Bonk, T. Bauer, Molten chloride salts for next generation CSP plants: electrolytical salt purification for reducing corrosive impurity level, Sol. Energy Mater. Sol. Cells 199 (2019) 8–15.
[52] K. Bawane, P. Manganaris, Y. Wang, J. Sure, A. Ronne, P. Halstenberg, S. Dai, S. K. Gill, K. Sasaki, Y.-ck. Chen-Wiegart, R. Gakhar, S. Mahurin, S.M. Pimblott, J. F. Wishart, L. He, Determining oxidation states of transition metals in molten salt corrosion using electron energy loss spectroscopy, Scripta Mater. 197 (2021), 113790.
[53] P. Sabharwall, D. Clark, M. Glazoff, G. Zheng, K. Sridharan, M. Anderson, Advanced heat exchanger development for molten salts, Nucl. Eng. Des. 280 (2014) 42–56.
[54] T.-F. Chen, G. Tiwari, Y. Iijima, K. Yamauchi, Volume and grain boundary diffusion of chromium in Ni-base Ni-Cr-Fe alloys, Mater. Trans. 44 (1) (2003) 40–46.
[55] A.U. Seybolt, Oxidation of Ni-20 Cr alloy and stainless steels in the presence of chlorides, Oxid. Met. 2 (2) (1970) 119–143.
[56] H. Ai, J. Hou, X.-X. Ye, C.L. Zeng, H. Sun, X. Li, G. Yu, X. Zhou, J.-Q. Wang, Influence of graphite-alloy interactions on corrosion of Ni-Mo-Cr alloy in molten fluorides, J. Nucl. Mater. 503 (2018) 116–123.
[57] H. Yin, J. Qiu, H. Liu, W. Liu, Y. Wang, Z. Fei, S. Zhao, X. An, J. Cheng, T. Chen, P. Zhang, G. Yu, L. Xie, Effect of CrF3 on the corrosion behaviour of Hastelloy-N and 316L stainless steel alloys in FLiNaK molten salt, Corros. Sci. 131 (2018) 355–364.
[58] D. Pradhan, G.S. Mahobia, K. Chattopadhyay, V. Singh, Effect of surface roughness on corrosion behavior of the superalloy IN718 in simulated marine environment, J. Alloy. Compd. 740 (2018) 250–263.
[59] J. Mitchell, N. Crow, A. Nieto, Effect of surface roughness on pitting corrosion of AZ31 Mg Alloy, Metals 10 (5) (2020).
[60] W.Y. Zhou, Y. Yang, G.Q. Zheng, K.B. Woller, P.W. Stahle, A.M. Minor, M.P. Short, Proton irradiation-decelerated intergranular corrosion of Ni-Cr alloys in molten salt, Nat. Commun. 11 (1) (2020).
[61] J. Snyder, P. Asanithi, A.B. Dalton, J. Erlebacher, Stabilized nanoporous metals by dealloying ternary alloy precursors, Adv. Mater. 20 (24) (2008) 4883 (+).
[62] W. Wang, B. Guan, X. Wei, J. Lu, J. Ding, Cellular automata simulation on the corrosion behavior of Ni-base alloy in chloride molten salt, Sol. Energy Mater. Sol. Cells 203 (2019), 110170.
[63] P. Bajpai, M. Poschmann, D. Andrš, C. Bhave, M. Tonks, M. Piro, Development of a new thermochemistry solver for multiphysics simulations of nuclear materials. In: The Minerals, Metals & Materials Society (eds) TMS 2020 149th Annual Meeting & Exhibition Supplemental Proceedings. The Minerals, Metals & Materials Series. Springer, Cham.
[64] A. Graham, R.R. Pillai, B.S. Collins, J.W. McMurray, Engineering scale molten salt corrosion and chemistry code development, Oak Ridge National Laboratory, 2020 (ORNL-SPR/2020/1582).